



Nanocomposites of graphene nanoplatelets in natural rubber: microstructure and mechanisms of reinforcement

Suhao Li¹, Zheling Li¹, Timothy L. Burnett², Thomas J. A. Slater², Teruo Hashimoto², and Robert J. Young^{1,*}

¹National Graphene Institute and School of Materials, University of Manchester, Oxford Road, Manchester M13 9PL, UK

²Henry Moseley X-ray Imaging Facility and School of Materials, University of Manchester, Oxford Road, Manchester M13 9PL, UK

Received: 22 March 2017

Accepted: 25 April 2017

Published online:

4 May 2017

© Springer Science+Business
Media New York 2017

ABSTRACT

The microstructure and mechanisms of reinforcement have been investigated in nanocomposites consisting of graphene nanoplatelets (GNPs) in natural rubber (NR). Nanocomposites with four different loadings of three different sized GNPs were prepared and were bench-marked against nanocomposites loaded with N330 carbon black. The microstructure of the nanocomposites was characterised through a combination of scanning electron microscopy, polarised Raman spectroscopy and X-ray computed tomography (CT), where it was shown that the GNPs were well dispersed with a preferred orientation parallel to the surface of the nanocomposite sheets. The mechanical properties of the nanocomposites were evaluated using tensile testing, and it was shown that, for a given loading, there was a three times greater increase in stiffness for the GNPs than for the carbon black. Stress transfer from the NR to the GNPs was evaluated from stress-induced Raman bands shifts indicating that the effective Young's modulus of the GNPs in the NR was of the order of 100 MPa, similar to the value evaluated using the rule of mixtures from the stress–strain data.

Introduction

Elastomers are used widely for various applications in many engineering sectors including automotive, aerospace, packaging and healthcare among others. This is based upon their wide range of attributes that include their ease of deformation at ambient temperatures, heat resistance and exceptional elongation and flexibility before breaking. Carbon-based nanomaterials such as carbon black have been used to

reinforce elastomers such as natural rubber for more than 100 years, giving rise to improvements in properties such as stiffness, strength and wear resistance [1–3]. More recently, high-performance elastomeric nanocomposites have been produced through the incorporation of other different types of inorganic fillers such as silica nanoparticles, layered silicates, multi-walled carbon nanotubes and other nanomaterials [4–11].

Address correspondence to E-mail: robert.young@manchester.ac.uk

There is currently a great deal of interest in the properties of graphene and other 2D materials [12–14]. It is well established that the Young's modulus of graphene is more than 1 TPa and it also has the highest level of strength ever measured for a material of over 130 GPa [15]. It is therefore not surprising that once graphene-based materials, such as graphene oxide and graphene nanoplatelets, became available in bulk, they would be considered for use in nanocomposites [16–21], with elastomers being obvious candidates as matrix materials. There are a number of reports of the reinforcement of different types of elastomer through the addition of graphene-based materials [22–40] that have recently been reviewed in detail by Papageorgiou et al. [41]. Although significant improvements in mechanical properties have been reported for graphene-reinforced elastomers, the mechanisms of reinforcement are still not yet fully understood.

In this present study, we have undertaken a detailed study of the mechanisms of reinforcement of natural rubber by graphene nanoplatelets. This has been undertaken by compounding natural rubber with different loadings of nanoplatelets of three different lateral dimensions and bench-marking these materials against natural rubber with different loadings of carbon black. The microstructure of the nanocomposites has been analysed using a range of state-of-the-art techniques such as polarised Raman spectroscopy [42, 43] and X-ray computed tomography [44–46] to give a unique insight into the microstructure of the materials. The effect of the different loadings of the nanomaterials upon the mechanical properties of the natural rubber has been evaluated. Stress transfer from the natural rubber matrix to the nanoplatelets has also been followed from stress-induced Raman band shifts during in situ deformation. This, along with the detailed microstructural analysis, has now enabled the mechanisms of reinforcement to be analysed in detail.

Experimental

Materials

The XG graphene nanoplatelets (termed GNPs) were purchased from XG Sciences Inc. Lansing, Michigan, USA, and used as received. Three types of Grade-M particles were employed with lateral diameters of

5 μm , 15 μm and 25 μm (designated as M5, M15 and M25, respectively). The thicknesses of all the flakes were quoted by the manufacturer to be in the range 6–8 nm (i.e. around 20 graphene layers). A carbon-based nanomaterial often used to reinforce elastomers, high-abrasion furnace HAF N330 carbon black (CB) supplied by the Berwin Polymer Processing Group, Duckinfield, UK, was employed for comparison with the GNPs.

The grade of natural rubber (NR) used was SMR CV60 (Standard Malaysian Rubber, Mooney-Viscosity ML (1 + 4, 100 °C) of 60). It was purchased from Astlett Rubber Inc., Oakville, Ontario, Canada, and used as received. All the additives involved in the rubber processing, zinc oxide, stearic acid, CBS accelerator and sulphur, were of analytical grade and used as received.

Preparation of GNP and CB natural rubber nanocomposites

The rubber mastication was conducted with a Bridge two-roll mill (manufactured by David Bridge & Co. Ltd) using the formulations listed in Table 1. Nominal loadings of 0, 5, 10, 15, 20 phr of the three different types of GNP and N330 CB were incorporated into the natural rubber matrix. Before the mixing, pieces of the rubber were pre-heated at 60 °C in an oven for 30 min to enable decrystallisation. The two-roll mill was set to a speed of 22 rpm with a friction ratio of 1.5:1 and a nip gap of 1 mm. For each batch of material, 200 g natural rubber was put in the two-roll mill and formed a sheet adhering to the surface of one of the rolls. When the rubber sheets became warm and sticky under rolling compaction, zinc oxide, stearic acid and CBS accelerator were added on to the rubber sheet. This was followed by mixing

Table 1 Formulation of the rubber compounds

Materials	Loading (phr ^a)
SMR CV60	100
Sulphur	3
CBS accelerator	1
Zinc oxide	3
Stearic acid	2.5
GNP and N330	5, 10, 15, 20

^a 'phr' is a preferred used unit in the rubber industry, abbreviation for "parts per hundred rubber"

for 10 min, during which time the rubber sheet was cut from one side and folded to the other side to achieve a good dispersion. Subsequently, the GNP or CB powder was gradually incorporated into the compound and followed by a similar mixing procedure for a time depending on the amount of additive. Finally, the sulphur was blended into the compound, with further mixing to achieve a uniform dispersion of all the additives in the natural rubber matrix and the mixing time was controlled to avoid the occurrence of premature vulcanisation.

The compounds were then cut into amounts corresponding to the designed mould dimensions and hot pressed in a metal mould into sheets (~ 2.5 mm thick) in a Collin platen press (Platenpress P 300 P/M). The vulcanisation proceeded at a temperature of 160 °C for 10 min under a hydraulic pressure of 30 bar.

Thermogravimetric analysis (TGA)

The actual fractions of GNP and CB in all the nanocomposites were determined by thermogravimetric analysis (TGA) in a TA Instruments Q500 TGA. The temperature range was set from room temperature to 800 °C using a heating rate of 40 °C/min in an atmosphere of nitrogen. The amounts of processing additives were presumed to be identical in the pure natural rubber and all the nanocomposites in determination of the mass fractions of the GNPs and CB in the rubber.

Scanning electron microscopy

The scanning electron microscopy (SEM) images of the GNPs and rubber nanocomposites were acquired using an EVO60 VPSEM (Zeiss) operated at 8–10 kV. The GNP particles and N330 CB were sprinkled on aluminium stubs before examination. SEM images of carbon black were obtained using a higher resolution XL 30 FEG Philips operated at 10 kV, the samples being coated with Au/Pd alloy before analysis. The microstructure of the nanocomposites was evaluated from low-temperature fracture surfaces. The samples were immersed into liquid nitrogen and broken by hand to produce well-defined brittle fracture surfaces. They were subsequently coated with Au/Pd alloy to render them conductive before being examined in the SEM.

Raman spectroscopy

Raman spectra were obtained from the materials using a Renishaw 2000 of Raman spectrometer with a laser length of 633 nm and a $\times 50$ objective lens in the microscope, giving a spot size of the order of 2 μm . The GNP and N330 CB particles were characterised from small clusters on glass slides. Raman spectra were also obtained from the low-temperature fracture surfaces of the nanocomposites.

The spatial orientation of graphene in rubber compound was determined as described before [42, 43]. In the orientation test, the Raman laser was aligned perpendicular to one surface of the rubber (either along the X or the Z axis as in Fig. 1), with the incident and scattered radiations polarised parallel to each other. The rotation angle in X and Z axis are denote as Φ_X and Φ_Z , respectively. The Raman G band of graphene was recorded, and its intensity as the function of the rotation angle Φ_X or Φ_Z is shown in Fig. 1. On the basis of the parameters determined from the orientation study, the orientation distribution function (ODF) of graphene in the rubber can be estimated. The angle between the surface normal of each graphene flake and the reference normal of the rubber piece is defined as θ , as illustrated in Fig. 2 in Ref. [43]. For example, if a graphene flake is in the plane of the rubber sheet, then $\theta = 0$.

The shifts of the Raman 2D band in the GNP/NR nanocomposites with strain were determined for the highest loadings (20 phr) of each type of GNP. This was undertaken using a tensile rig to clamp the rubber strip specimens and provide a static tensile force. The strain was determined from the change in separation of the grips. A VN laser polarisation configuration (vertically-polarised incident light and unpolarised scattered light) was used and the laser beam focused on individual flakes exposed on the surface of each specimen. Spectra were obtained at static strains of 0, 30, 40, 60, 80, 90, 120 and 160%. At least 8 different specimens were tested for each of the GNP/NR materials.

X-ray computed tomography

Samples for X-ray CT were prepared using a Leica Ultracut UC6 Ultramicrotome. Sections of the moulded sheets were sandwiched between two aluminium plates for cutting and were microtomed at an

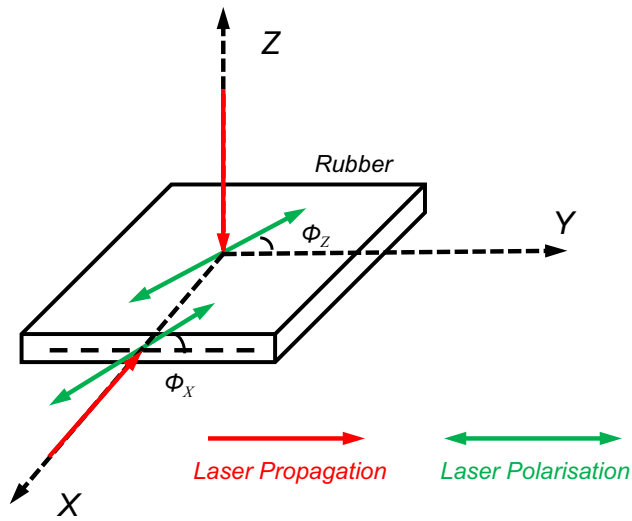


Figure 1 Experimental arrangement for the study of GNP orientation using Raman spectroscopy.

angle along three directions, leaving the moulded surface face intact.

Nanoscale X-ray CT data were acquired on a Zeiss Xradia Ultra 810 instrument, which employs a fixed energy of 5.5 keV (Cr target). Projections for each sample were acquired in phase contrast and ‘large field of view’ mode with a 30 s exposure time, 801 projections and a pixel size of 128 nm. The series

were reconstructed with a filtered back projection reconstruction through the Zeiss XMReconstructor software (version 9.1.12862).

All visualisation and thresholding was performed in the Avizo software package (version 9.1.1). Segmentation was performed through global thresholding (at different intensity values for each reconstruction), followed by removal of ‘islands’ of volume less than 500 pixels. The surface area and the orientation of each flake were calculated through use of the Avizo ‘Label Measures’. To calculate the orientation of each flake, the angles corresponding to the ‘length’, the longest flake dimension (calculated over 91 angles in 3D), and the ‘breadth’, the longest flake dimension perpendicular to the ‘length’ (calculated over 90 angles in the plane perpendicular to the length), were first obtained. The polar angles of the direction perpendicular to the ‘length’ and ‘breadth’, corresponding to the direction normal to the flake, was calculated by taking the cross-product of unit vectors at the angles corresponding the ‘length’ and ‘breadth’ for each flake. The angle between the normal to the flake and the normal to the pressed surface was obtained by calculating the dot-product of the unit vector corresponding to each direction.

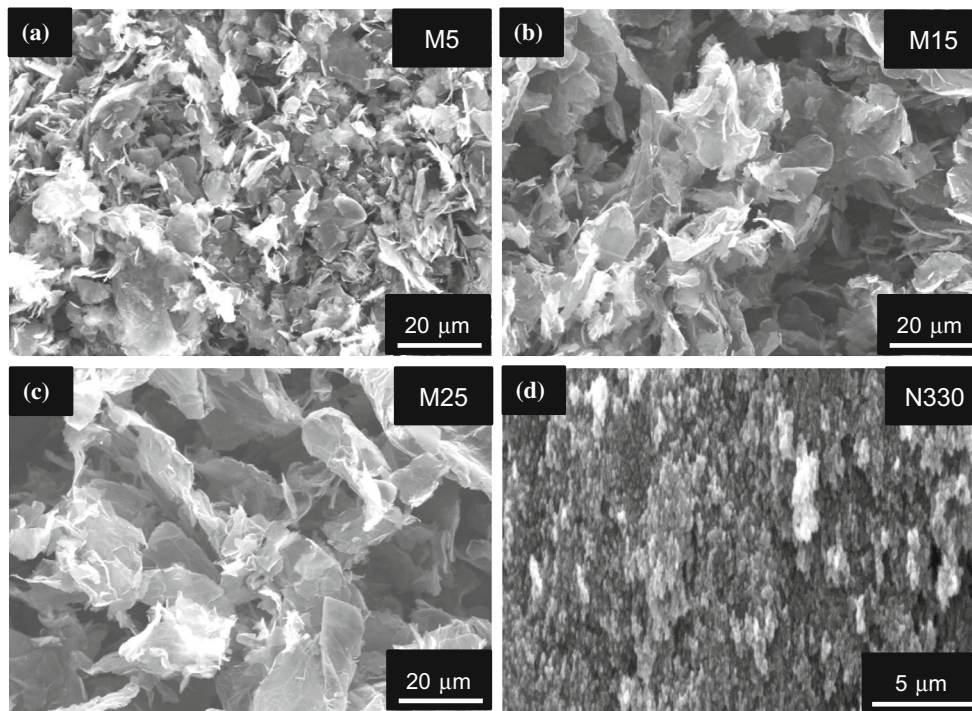


Figure 2 SEM micrographs of the particles, a M5, b, M15, c M25 and d N330 carbon black.

Mechanical testing

Tensile testing was undertaken using an Instron-1122 universal testing machine. The specimens were prepared by cutting the 2.5-mm-thick sheets into a dumbbell shape with a gauge length of 25 mm and a width of 4 mm. Prior to testing, the specimens were conditioned by being placed in a climate-controlled laboratory for 24 h at a temperature of 23.0 ± 0.1 °C and a relative humidity of $50 \pm 5\%$. For each formulation, five specimens were tested and deformed at a crosshead speed of 500 mm/min until fracture. The strain was measured from the change in grip separation.

Hardness testing

The hardness tests were conducted using a Shore A durometer (Duratool 59-500-000 Durometer Shore 'A' Scale, manufactured to the standards DIN 53505/ASTM D2240). The durometer was held in a vertical position with the indenter point at least 12 mm from the specimen edge, followed by the pressure foot being applied to the specimen as rapidly as possible, without shock. The hardness values were obtained from the stop hand retained at the hardness reading. The tests were undertaken at $23^\circ\text{C} \pm 2^\circ\text{C}$, and 5 specimens were measured for each composition using the procedure detailed above.

Results

Characterisation of the GNPs and carbon black

Scanning electron microscopy (SEM)

Scanning electron micrographs of the three different types of GNPs and of the N330 carbon black are shown in Fig. 2. It can be seen that the GNPs have a high aspect ratio with a systematic increase in flake size going from M5 to M15 to M25. The morphology of the N330 is, however, quite different consisting of agglomerates of nano-sized particles of the order of 30–35 nm in diameter, near to the resolution limit of the scanning electron microscope.

Raman spectroscopy

Representative Raman spectra of the three types of GNPs, carbon black and natural rubber are presented in Fig. 3a. It can be seen that the GNPs all show a weak D band and well-defined G and 2D bands indicative of a graphitic structure. In contrast, the N330 carbon black has two very broad and overlapping D and G bands and no 2D band, consistent with a highly-disordered amorphous carbon structure. No well-defined Raman spectrum can be obtained from the natural rubber, and it shows only a very broad peak resulting from background fluorescence. Raman spectra for the NR filled with 20 phr of the three different types of GNPs are shown in Fig. 3b. It can be seen that they appear similar to the spectra for the GNPs in Fig. 3a, but the relative intensity of the D band is slightly higher than in the spectra of the GNPs before processing. There is also a fluorescent background from the rubber matrix. The spectrum obtained from the carbon black in the natural rubber was similar to that for the carbon black alone, but had broader D and G bands.

Characterisation of the nanocomposites

Thermogravimetric analysis (TGA)

Thermogravimetric analysis was undertaken to determine the actual compositions of the natural rubber nanocomposites since the processing method employed inevitably involves some loss of filler material. In addition, there were also other additives in the rubber (see Table 1) that needed to be taken into account. The mass fractions of the GNPs and carbon black in the natural rubber determined from TGA are summarised in Table 2. The volume fractions, calculated using the appropriate densities of the rubber, filler and additives are also given in the Table.

Scanning electron microscopy

The distribution and orientation of the GNPs and carbon black in the natural rubber was evaluated firstly using SEM of samples of the fractured rubber sheets after immersion in liquid nitrogen. Examples of the fracture surfaces for the materials loaded with 15phr of the fillers are given in Fig. 4. Flakes of the GNPs can clearly be seen to be well distributed in the natural rubber matrix and protruding from the surfaces

Figure 3 Raman spectra of the materials studied.

a Starting materials and **b** nanocomposites.

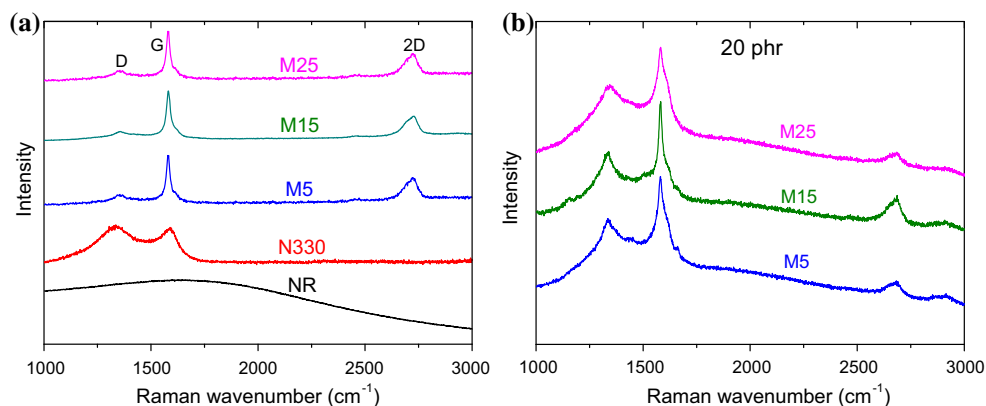


Table 2 Mass fractions of the GNPs and carbon black in the natural rubber determined from thermogravimetric analysis, along with the estimated volume fractions

Material	Mass fraction (%)	Volume fraction (%)
NR	0	0
M5 5 phr	3.55 ± 0.35	1.57 ± 0.15
M5 10 phr	7.10 ± 0.41	3.22 ± 0.18
M5 15 phr	10.64 ± 0.35	4.92 ± 0.15
M5 20 phr	14.19 ± 0.06	6.71 ± 0.03
M15 5 phr	3.18 ± 0.19	1.41 ± 0.08
M15 10 phr	7.34 ± 0.32	3.33 ± 0.14
M15 15 phr	10.76 ± 0.17	4.98 ± 0.07
M15 20 phr	13.31 ± 0.58	6.26 ± 0.25
M25 5 phr	3.70 ± 0.14	1.64 ± 0.06
M25 10 phr	6.88 ± 0.30	3.11 ± 0.13
M25 15 phr	10.21 ± 0.24	4.71 ± 0.10
M25 20 phr	13.21 ± 0.09	6.21 ± 0.04
CB 5 phr	3.64 ± 0.14	1.97 ± 0.08
CB 10 phr	7.44 ± 0.18	4.10 ± 0.10
CB 15 phr	11.27 ± 0.12	6.32 ± 0.06
CB 20 phr	14.67 ± 0.08	8.38 ± 0.04

for the M5, M15 and M25 materials, whereas the fracture surface for the sample containing the N330 NBR is much smoother and sub-micron-sized clusters of carbon black agglomerates can just about be resolved in the surface features. Preferred alignment of the GNPs in the plane of the sheets (horizontal) can also be seen in Fig. 4a–c. Representative fracture surfaces of the unfilled rubber and 5, 10 and 20 phr of the GNPs and carbon black showing similar characteristics are also presented in the Supplementary Information.

Polarised Raman spectroscopy

Since the fracture surfaces of the GNPs nanocomposites showed preferred alignment of the GNPs,

polarised Raman spectroscopy was employed to quantify the level of orientation of the GNPs in the nanocomposites. The results of this analysis are shown in Fig. 5 where the measurements of the intensity of the G band as a function of orientation rotating each specimen around the Z and X axes are presented for the natural rubber with 20 phr of the three different GNPs. It can be seen that in each case there is no change in intensity during rotation of the specimen about the Z axis (perpendicular to the sheet), implying no preferred orientation of the GNPs in the X or Y directions (illustrated in Fig. 1). In contrast, it can be seen that in each case the intensity of the G band decreases with increasing angle of rotation when the specimens were rotated about the X axis (similar behaviour was found for rotation about the Y axis). This implies that GNPs tend to be aligned in-plane within the natural rubber sheets. It is possible to quantify this level of orientation from the values of $\langle P_2(\cos \theta) \rangle$ and $\langle P_4(\cos \theta) \rangle$ [42] fitted to the data in Fig. 5, and they are also given on the plots. It can be seen that $\langle P_2(\cos \theta) \rangle$ and $\langle P_4(\cos \theta) \rangle$ decrease going from M5 to M15 to M25 implying a lower degree of orientation for the larger GNPs, possibly as a result of the presence of folds and loops in the larger particles (see next). It should be pointed out that $\langle P_2(\cos \theta) \rangle = 1$ for perfect alignment and $\langle P_2(\cos \theta) \rangle = 0$ for random orientation [43]. The value of $\langle P_2(\cos \theta) \rangle$ was found to be in the range 0.2–0.7 for all the 12 GNP nanocomposite samples studied (5, 10, 15 and 20 phr of M5, M15 and M25 GNPs), showing a general preferred in-plane alignment of the nanoplatelets. No systematic trend could, however, be found with either the level of loading or particle size. This is most likely due to the fact that the size of the Raman laser spot ($\sim 2 \mu\text{m}$) is of the same order of

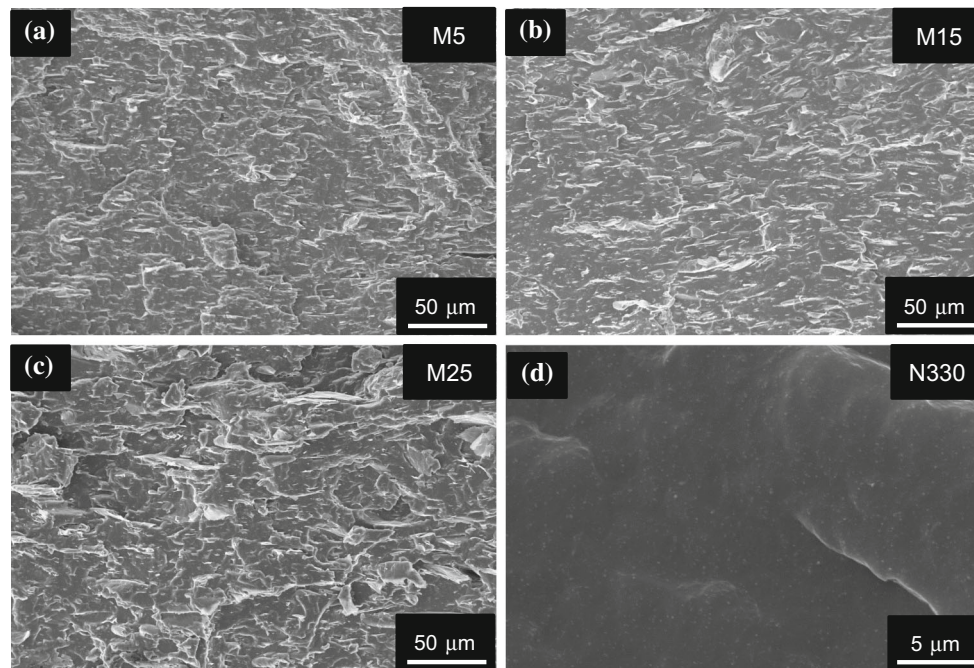


Figure 4 SEM micrographs of fracture surfaces of the nanocomposites at 15 phr loading.

magnitude as the lateral size of the GNPs. A large number of orientation measurements would therefore have to be made on each sample to obtain statistically significant results.

X-ray computed tomography

X-ray computer nanotomography was also used to characterise the distribution and orientation of the GNPs in the nanocomposites as shown in Fig. 6. It can be seen that the GNPs are well distributed within the rubber matrix with preferential alignment, as seen in the SEM micrographs. Moreover, the nanotomography technique gives unprecedented detail of the morphology of the GNPs showing that many are bent into loops, although their overall dimensions are consistent with their nominal size specifications. More detail of the distributions of the GNPs throughout the samples can be seen in stills, and in the movies of the slices through the nanocomposites in the Supplementary Information, along with volume rendered images.

Mechanical properties

Stress–strain behaviour

Stress strain curves for all the materials studied are given in Fig. 7. Five stress–strain curves were

obtained for each loading level for each type of filler, and representative ones are presented. Overall the addition of the GNPs and carbon black can be seen to increase the stiffness of the materials significantly. Natural rubber has a relatively high inherent strength, because of its tendency to strain crystallise, and none of the fillers appear to increase its strength. The strength of the natural rubber appears to be maintained for the M5 and CB fillers but decreases somewhat in the case of the addition of the larger M15 and M25 GNPs. It may be possible, however, to the increase strength using functionalised fillers that improve the strength of the rubber–filler interface. In all cases, the strain at failure appears to be reduced by the addition of the different types of filler.

Modulus values

The effect of the addition of the different fillers upon the stiffness of the rubber is shown in detail in Fig. 8. Although there does not appear to be large difference in the overall stress–strain curves between the GNPs and CB fillers in Figs. 7, 8a shows that for the 20 phr loading the shapes of the stress–strain curves are quite different at low strain (<300%). The addition of the GNPs leads to a significantly higher initial slope for the stress–strain curve than for the rubber reinforced with carbon black, so that the modulus at

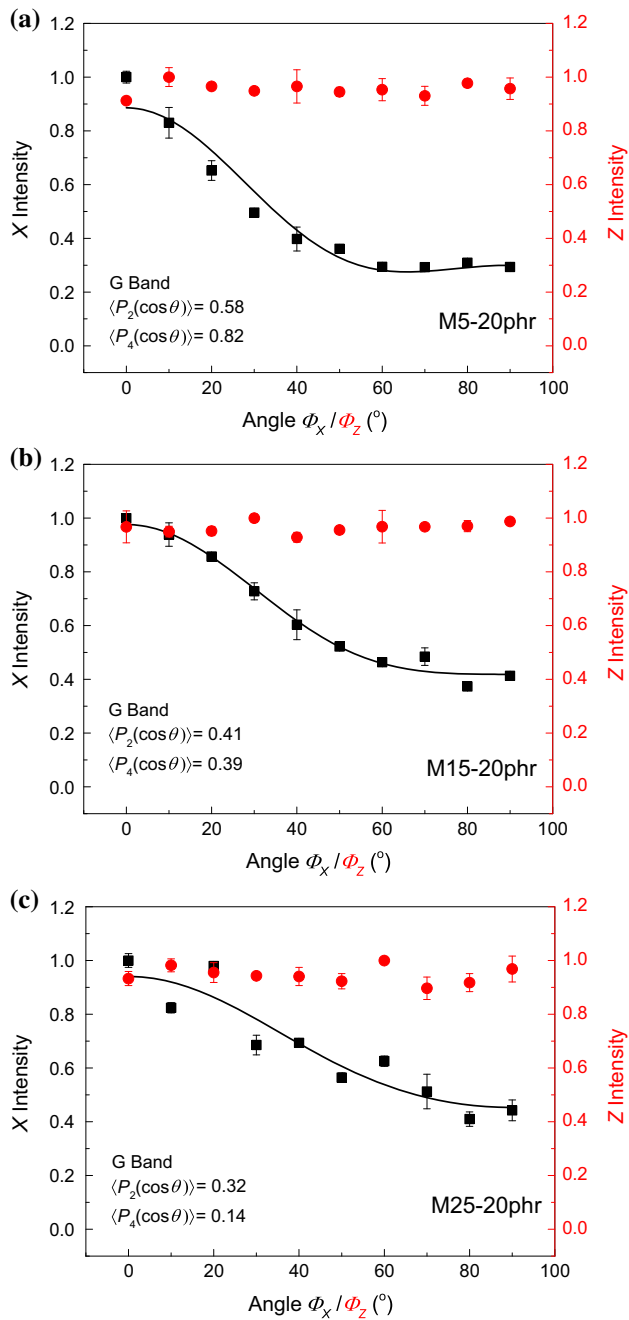


Figure 5 Polarised Raman measurements of the intensity of the G band as a function of orientation around the Z and X axes for the natural rubber with 20 phr of **a** M5, **b** M15 and **c** M25 GNPs.

100% strain is more than twice that of the carbon black loaded material. Similar behaviour was found for the other levels of filler loading.

The tensile moduli at 100 and 200% strain are plotted as a function of the volume fraction of fillers (Table 2) in Fig. 8b, c, respectively. The higher levels of reinforcement achieved with the addition of the

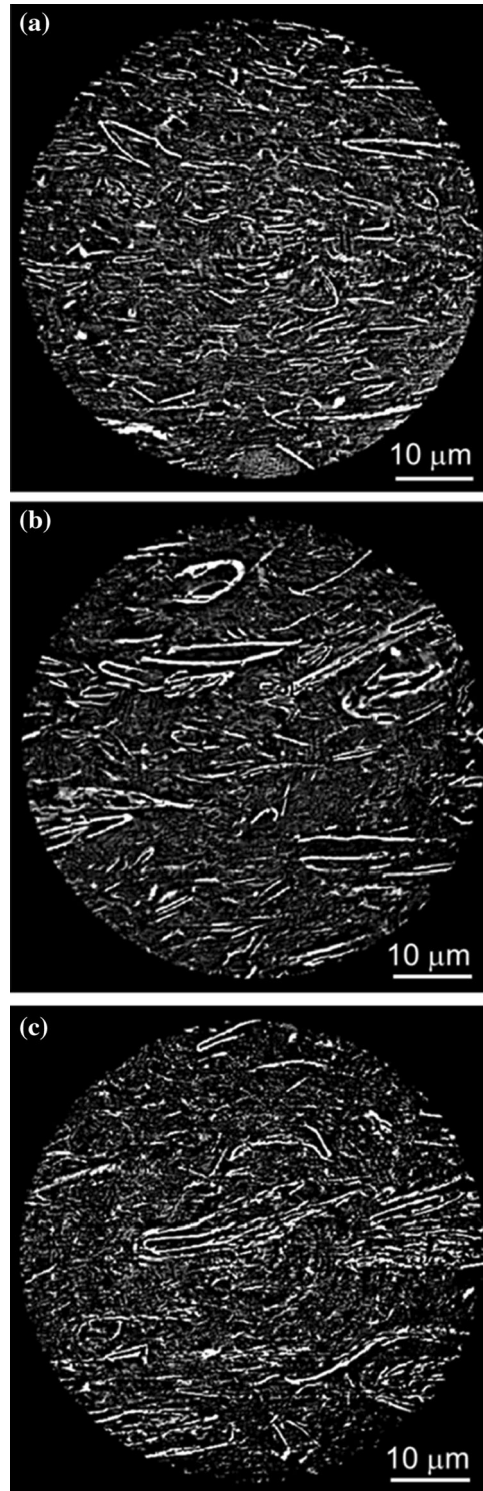


Figure 6 Slices through CT reconstructed volumes (print—stills; SI—videos) showing details of structure, distribution and orientation of the GNPs in the natural rubber nanocomposites at 20 phr loading for **a** M5, **b** M15, **c** M25. (The surface of the sheet is horizontal, and the small *white spots* in the micrographs are from the zinc oxide added to aid the vulcanization of the rubber).

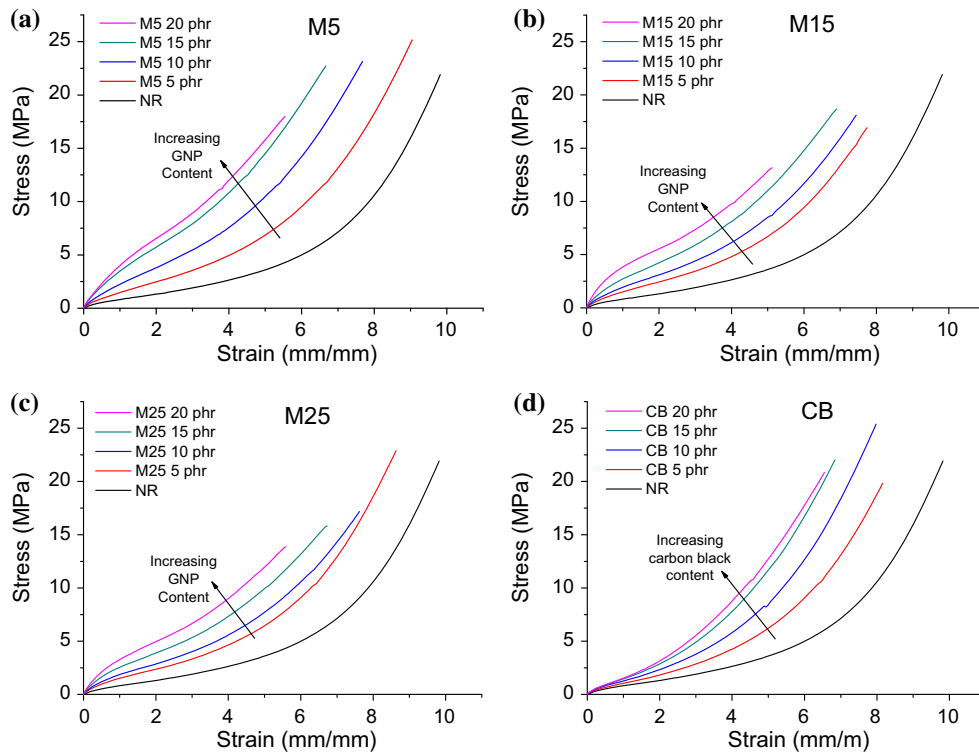


Figure 7 Stress–strain curves for the natural rubber containing 5, 10, 15 and 20 phr of **a** M5, **b** M15, **c** M25 and **d** N330 carbon black.

Figure 8 Mechanical properties of the nanocomposites.

a Comparison of the stress–strain curves for the different nano-fillers at 20 phr loading.

b Tensile modulus at 100% strain as a function of filler volume fraction.

c Tensile modulus at 200% strain as a function of filler volume fraction.

d Shore A hardness as a function of filler volume fraction.

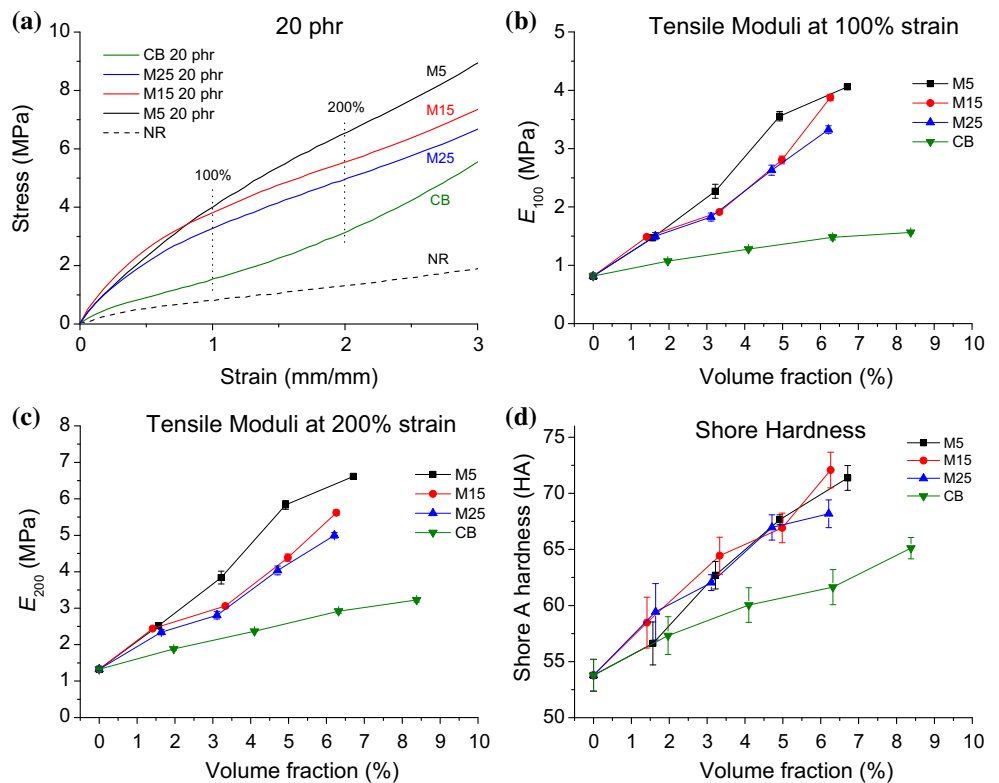
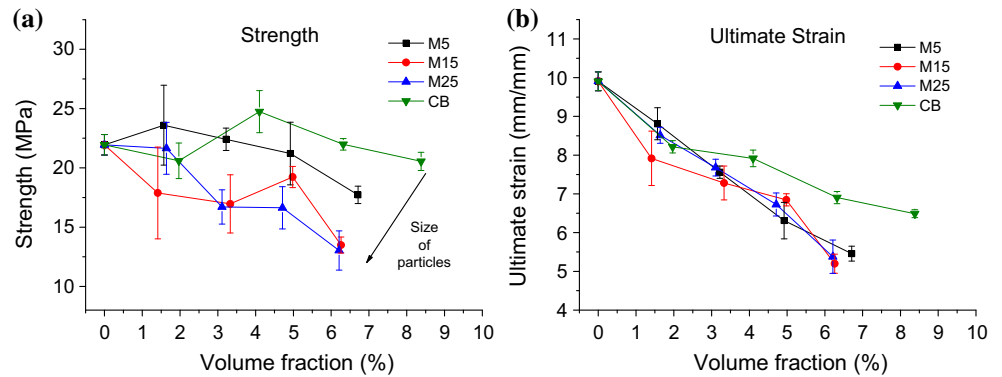


Figure 9 Mechanical properties of the nanocomposite as a function of filler volume fraction. **a** Tensile strength and **b** ultimate strain.



GNPs compared with that obtained for the CB at a given volume fraction can be clearly seen. There also seems to be a slightly better reinforcement of the rubber for the M5 GNPs compared with the M15 or M25 fillers. Another way of looking at the data in Fig. 8b, c is in terms of the volume fraction of filler needed for a particular level of modulus. It can be seen that for a particular modulus value, up to three times the volume fraction of carbon black is needed to match that of natural rubber reinforced with the GNP materials.

Finally the Shore hardness of sheets of the natural rubber and all materials with different filler loadings was determined as shown in Fig. 8d and it can be seen that the measured values of Shore hardness mirror the dependence of the 100 and 200% modulus values upon the type and loading of filler shown in Fig. 8b, c.

Ultimate properties

It was pointed out earlier that since natural rubber crystallises under stress, it is relatively strong. Figure 9a shows that the strength is unaffected by the addition of the carbon black but tends to decrease slightly on the addition of the GNPs, with the largest particles giving rise to the highest level of strength reduction. Figure 9b shows the effect of the addition of GNPs and CB upon the ultimate failure strain of the natural rubber. It decreases with filler loading, with all three GNP materials showing the same behaviour. In contrast, the addition of carbon black

causes rather less reduction in failure strain, particularly for the higher volume fractions.

The effect of the different nano-fillers upon the ultimate properties of the natural rubber appears to be related to the size of the particles. This implies that the particles act as defects in nucleating cracks. Hence, the largest GNP particles, M15 and M25, cause the highest decrease in strength with increasing volume fraction (Fig. 9a), whereas the strength appears to be maintained upon the addition of the carbon black.

Stress-induced Raman band shifts

Shifts in the position of the 2D Raman band with strain were determined for the NR filled with the three different GNP materials, as shown in Fig. 10. This was a particularly difficult experiment to undertake as the 2D band is rather ill-defined in the spectrum as a result of fluorescence from the NR matrix, as found in Fig. 3b, and the shifts were relatively small. Hence only the materials with the highest loading of 20 phr of GNPs were employed as they had the strongest 2D band. Additionally, as the result of the small band shifts and scatter in the data, the experiments were undertaken upon at least 8 different specimens for each composition and the data points in Fig. 10 represent the mean values for all the specimens used for each type of GNP.

Although there is considerable scatter in the data in Fig. 10 and relatively large error bars, it appears that there is a small but significant downshift in the

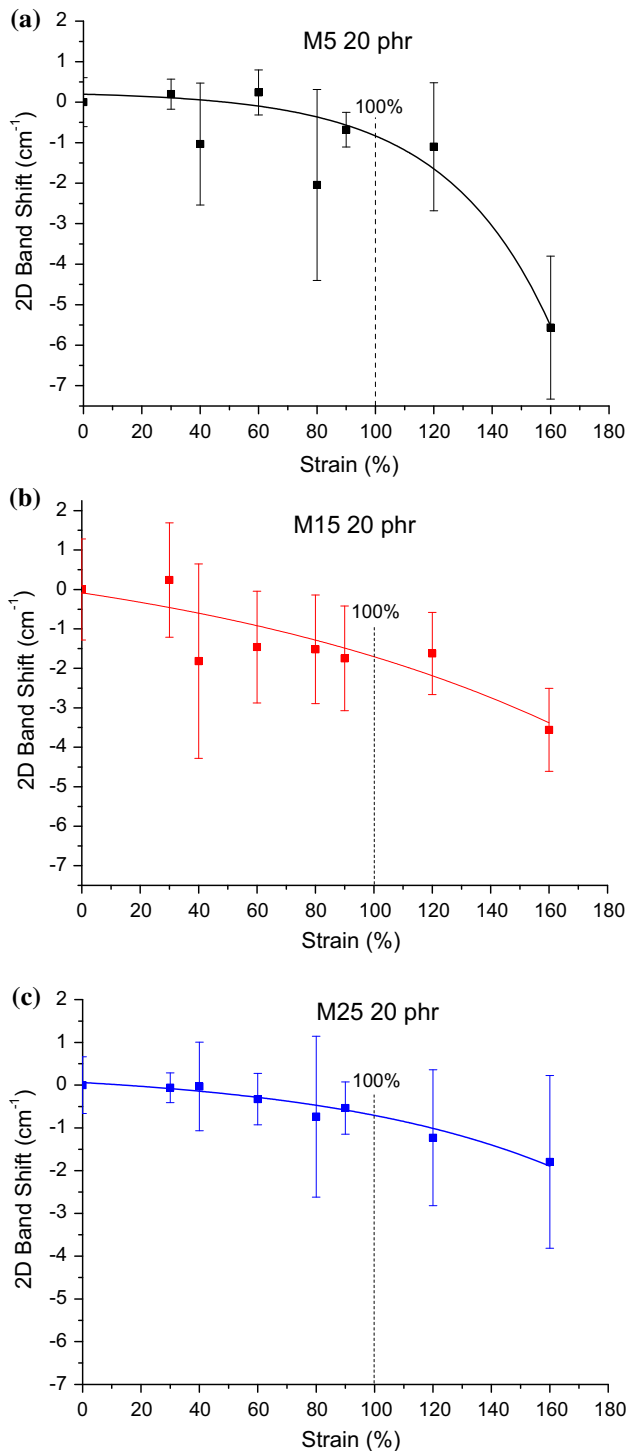


Figure 10 Shift of the 2D Raman band with strain for the nanocomposites with 20 phr of **a** M5, **b** M15 and **c** M25.

position of the 2D band with tensile strain. For each type of filler, the data were fitted to non-linear exponential curves that all show an increasing shift rate as the strain increases.

Discussion

Microstructure

In this study two techniques, polarised Raman spectroscopy and X-ray computed tomography, have been employed for the first time to characterise the microstructure of graphene-based nanocomposites. They have given unprecedented levels of information about the orientation and distribution of the GNPs in natural rubber. Even though the individual GNPs are only of the order of 6–8 nm thick it has been shown that it is possible to visualise them individually within the nanocomposites using X-ray CT through Zernike phase contrast imaging. One feature that is immediately revealed in the GNPs in Fig. 6 is their folded and looped structures, as well as multiple stacking. Overall it appears that the GNPs have not been fragmented during processing and the alignment of the GNPs, approximately parallel to the surface of the nanocomposite sheets, probably induced by the hot pressing procedure, is clear. The level of alignment is also apparent from the polarised Raman spectroscopy analysis (Fig. 5) which we have demonstrated can also be quantified in terms of orientation distribution functions using this technique.

It will be shown next how the quantitative assessment of the level of orientation can be used in the interpretation of the mechanisms of deformation in the nanocomposites.

Mechanisms of reinforcement

One of the simplest methods of evaluating the reinforcement achieved in nanocomposites is the ‘rule of mixtures’ [47] whereby the Young’s modulus of the nanocomposite E_c is given by the relationship

$$E_c = E_f V_f + E_m V_m \quad (1)$$

where E_f , E_m are the effective modulus of the filler and the modulus of the matrix, while V_f and V_m are the volume fractions of the filler and the natural rubber matrix. The value of the effective modulus of the fillers can be determined directly from the slopes of the lines in Fig. 8c for the modulus values at 100% strain. The derived values of E_f for the different GNPs and carbon black are given in Table 3, and it can be seen that E_f is significantly higher for the GNPs than the carbon black.

Table 3 Modulus at 100% strain for the natural rubber and nanocomposites for a volume fraction of 5% filler determined from Fig. 8c

	NR ^a	N330	M5	M15	M25
E_{100} at $V_f = 5\%$ (MPa)	0.81 ± 0.04	1.36 ± 0.08	3.55 ± 0.18	2.78 ± 0.16	2.74 ± 0.16
E_f (MPa)	–	11	55	39	39
η_o	–	–	0.825	0.725	0.670
E_{eff} (MPa)	–	–	67 ± 15	54 ± 11	58 ± 12

E_f is the modulus of the filler determined using the rule of mixtures, η_o is the Krenchel orientation factor determined from the parameters in Fig. 5, and E_{eff} is the effective modulus of the graphene determined using Eq. (2)

^a Data for unfilled NR

Table 4 Shift of the 2D Raman band determined for each of the GNP nanocomposites at 100% strain

	M5	M15	M25
Band shift at 100% strain (cm^{-1})	-0.85 ± 0.29	-1.71 ± 0.58	-0.71 ± 0.24
E_{eff} (MPa)	150 ± 50	300 ± 100	125 ± 40

As mentioned earlier, the orientation and size of a platelet-like filler plays a major role in the reinforcement, and for this reason a modified rule of mixtures has been proposed [43]:

$$E_c = E_{eff} V_f \eta_o \eta_l + E_m V_m \tag{2}$$

where E_{eff} is now the effective modulus of the GNPs and η_o is the Krenchel orientation factor which depends on the average orientation of the filler with respect to the applied stress. The parameter η_l is the length distribution factor and takes values between 0 and 1. It is possible to take into account the effect of orientation to determine the effective modulus of the GNPs by dividing E_f by η_o determined from the orientation parameters in Fig. 5 [43] and the values of E_{eff} determined (assuming at this stage $\eta_l = 1$) are of the order of 60 MPa as shown in Table 3.

The effective modulus of the graphene can be also be estimated completely independently from the stress-induced Raman band shifts shown in Fig. 10. It is well established [17] that the 2D bands of a graphene monolayer with a Young’s modulus 1050 GPa [15] will undergo a shift of -60 cm^{-1} when deformed to a strain of 1%. This observation allows the effective modulus of any type of graphene under tensile stress to be determined in a variety of microstructures, including nanocomposites, from stress-induced shifts of the 2D band. The effective modulus of the GNPs in the nanocomposites is therefore given by

$$E_{eff} = - \frac{d\omega_{2D}}{d\varepsilon} \frac{1050}{-60} \text{GPa} \tag{3}$$

where $-d\omega_{2D}/d\varepsilon$ is the shift rate of the 2D Raman band in the nanocomposite in $\text{cm}^{-1}/\%$ strain. The shift rates measured for the nanocomposites in this present study were very small, as can be seen in Fig. 10, typically around -1 cm^{-1} for 100% strain ($E_{eff} \sim 175 \text{ MPa}$), indicating that the effective modulus of the GNPs in the NR is relatively small compared with that of pristine graphene (1050 GPa). The 2D band shifts for the GNPs at 100% strain measured for the nanocomposites with 20 phr of GNPs are listed in Table 4 and the values of E_{eff} calculated using Eq. (3) are given in the Table. It can be seen that the derived values of E_{eff} are in the range 125–300 MPa, but there is considerable scatter in the data.

It is interesting to consider why the Raman analysis gives a higher value of effective Young’s modulus of the GNPs in the NR than the mechanical testing data, and why both values are many orders of magnitude lower than the value of 1050 GPa for pristine graphene [15]. The Raman measurements were made upon individual exposed GNP flakes under stress in the nanocomposites, whereas the mechanical data were obtained for the deformation of the whole nanocomposite. We have not so far taken into account any length effects that will reduce the effectiveness of the reinforcement by the GNPs ($\eta_l < 1$). The difference between the values of E_{eff} determined using the two techniques could be rationalised through using a value of η_l of the order of 0.3 for the values determined by mechanical testing.

In any case, both effective modulus values are 4 orders of magnitude lower than that of the pristine graphene. This indicates that although impressive levels of reinforcement can be obtained through the use of GNPs in NR, stress transfer from the NR to the GNPs that takes place through the NR/GNP interface by shear of the low modulus NR matrix [48] is relatively inefficient. This means that the full potential of reinforcement by the GNPs is difficult to achieve in such soft systems.

Conclusions

A new insight has been found into the microstructure and mechanisms of reinforcement in natural rubber reinforced with graphene nanoplatelets. The use of state-of-the-art techniques such as polarised Raman spectroscopy and X-ray CT has enabled detailed information to be obtained about the orientation and microstructure of the GNPs in the nanocomposites. Some of the GNPs were found to be in folded and looped structures, and multiple stacking of the nanoplatelets was sometimes observed. It has also been found that the GNPs were not fragmented during processing and that there was alignment of the GNPs approximately parallel to the surface of the nanocomposite sheets, probably as a result of the hot pressing procedure employed during processing.

It has been demonstrated that for a given loading of filler in natural rubber, the GNPs can give up to a three times better increase in stiffness than N330 carbon black. Since natural rubber is a relatively strong elastomer, its strength was not increased by the addition of the GNPs. Stress transfer from the natural rubber to the GNPs has been determined from stress-induced Raman band shifts. Although these shifts are relatively small, it has been shown that the effective Young's modulus of the graphene is of the order of 100 MPa. This was shown to be consistent with that determined from the analysis of the stress–strain data from tensile testing. This value of effective Young's modulus is, however, four orders of magnitude less than the generally accepted value of 1050 GPa for monolayer graphene. It has been proposed that this discrepancy is primarily the result of the inefficiency of stress transfer from the low modulus natural rubber matrix to the high-modulus filler by shear at the GNP/NR interface.

Supplementary information

Scanning Electron Microscopy (SEM): fracture surfaces of the natural rubber, fracture surfaces of the nanocomposites with different loadings of N330 carbon black, fracture surfaces of the nanocomposites with different loadings of GNPs. *X-ray Computed Tomography*: slices through CT reconstructed volumes showing details of structure, distribution and orientation of the GNPs, artificially coloured volume renderings of the individual segmented GNP flakes, videos of Fig. 6a–c.

Acknowledgements

This research has been supported by funding from the European Union Seventh Framework Programme under Grant Agreement No. 604391, the Graphene Flagship. The authors would like to acknowledge EPSRC funding of the Henry Moseley X-ray Imaging Facility (EP/F007906; EP/F001452; EP/I02249X), in addition to HEFCE funding through the UK Research Partnership Investment Funding (UKRPIF) Manchester RPIF Round 2 for the Multiscale Characterisation Facility.

Compliance with ethical standards

Conflicts of interest The authors have no conflicts of interest related to this work.

Electronic supplementary material: The online version of this article (doi:[10.1007/s10853-017-1144-0](https://doi.org/10.1007/s10853-017-1144-0)) contains supplementary material, which is available to authorized users.

References

- [1] Donnet JB, Voet A (1976) Carbon black: physics, chemistry and elastomer reinforcement. Marcel Dekker, New York
- [2] Edwards DC (1990) Polymer-filler interactions in rubber reinforcement. *J Mater Sci* 25:4175–4185. doi:[10.1007/bf00581070](https://doi.org/10.1007/bf00581070)
- [3] Boonstra BB (1979) Role of particulate fillers in elastomer reinforcement: a review. *Polymer* 20:691–704. doi:[10.1016/0032-3861\(79\)90243-X](https://doi.org/10.1016/0032-3861(79)90243-X)
- [4] Koerner H, Price G, Pearce NA, Alexander M, Vaia RA (2004) Remotely actuated polymer nanocomposites–stress-

- recovery of carbon-nanotube-filled thermoplastic elastomers. *Nat Mater* 3:115–120. doi:[10.1038/nmat1059](https://doi.org/10.1038/nmat1059)
- [5] Leblanc JL (2002) Rubber–filler interactions and rheological properties in filled compounds. *Prog Polym Sci* 27:627–687. doi:[10.1016/S0079-6700\(01\)00040-5](https://doi.org/10.1016/S0079-6700(01)00040-5)
- [6] Frogley MD, Ravich D, Wagner HD (2003) Mechanical properties of carbon nanoparticle-reinforced elastomers. *Compos Sci Technol* 63:1647–1654. doi:[10.1016/S0266-3538\(03\)00066-6](https://doi.org/10.1016/S0266-3538(03)00066-6)
- [7] Donnet JB (2003) Nano and microcomposites of polymers elastomers and their reinforcement. *Compos Sci Technol* 63:1085–1088. doi:[10.1016/S0266-3538\(03\)00028-9](https://doi.org/10.1016/S0266-3538(03)00028-9)
- [8] Joly S, Garnaud G, Ollitrault R, Bokobza L, Mark JE (2002) Organically modified layered silicates as reinforcing fillers for natural rubber. *Chem Mater* 14:4202–4208. doi:[10.1021/cm020093e](https://doi.org/10.1021/cm020093e)
- [9] Ponnamma D, Sadasivuni KK, Grohens Y, Guo Q, Thomas S (2014) Carbon nanotube based elastomer composites—an approach towards multifunctional materials. *J Mater Chem C* 2:8446–8485. doi:[10.1039/c4tc01037j](https://doi.org/10.1039/c4tc01037j)
- [10] Sherif A, Izzuddin Z, Qingshi M, Nobuyuki K, Andrew M, Hsu-Chiang K, Peter M, Jun M, Liqun Z (2013) Melt compounding with graphene to develop functional, high-performance elastomers. *Nanotechnology* 24:165601. doi:[10.1088/0957-4484/24/16/165601](https://doi.org/10.1088/0957-4484/24/16/165601)
- [11] Basu D, Das A, Stöckelhuber KW, Wagenknecht U, Heinrich G (2014) Advances in layered double hydroxide (LDH)-based elastomer composites. *Prog Polym Sci* 39:594–626. doi:[10.1016/j.progpolymsci.2013.07.011](https://doi.org/10.1016/j.progpolymsci.2013.07.011)
- [12] Novoselov KS, Geim AK, Morozov S, Jiang D, Zhang Y, Dubonos S, Grigorieva I, Firsov A (2004) Electric field effect in atomically thin carbon films. *Science* 306:666–669. doi:[10.1126/science.1102896](https://doi.org/10.1126/science.1102896)
- [13] Novoselov KS, Geim AK, Morozov SV, Jiang D, Katsnelson MI, Grigorieva IV, Dubonos SV, Firsov AA (2005) Two-dimensional gas of massless Dirac fermions in graphene. *Nature* 438:197–200. doi:[10.1038/nature04233](https://doi.org/10.1038/nature04233)
- [14] Geim AK, Novoselov KS (2007) The rise of graphene. *Nat Mater* 6:183–191. doi:[10.1126/science.1102896](https://doi.org/10.1126/science.1102896)
- [15] Lee C, Wei X, Kysar JW, Hone J (2008) Measurement of the elastic properties and intrinsic strength of monolayer graphene. *Science* 321:385–388. doi:[10.1126/science.1157996](https://doi.org/10.1126/science.1157996)
- [16] Young RJ, Kinloch IA (2013) Graphene and graphene-based nanocomposites. *Nanosci-Spec Per Rep* 1:145–179. doi:[10.1039/9781849734844-00145](https://doi.org/10.1039/9781849734844-00145)
- [17] Young RJ, Kinloch IA, Gong L, Novoselov KS (2012) The mechanics of graphene nanocomposites: a review. *Compos Sci Technol* 72:1459–1476. doi:[10.1016/j.compscitech.2012.05.005](https://doi.org/10.1016/j.compscitech.2012.05.005)
- [18] Young RJ (2016) Graphene and graphene-based nanocomposites. *Cism Courses Lect* 563:75–98. doi:[10.1007/978-3-7091-1887-0_4](https://doi.org/10.1007/978-3-7091-1887-0_4)
- [19] Young RJ, Liu MF (2016) The microstructure of a graphene-reinforced tennis racket. *J Mater Sci* 51:3861–3867. doi:[10.1007/s10853-015-9705-6](https://doi.org/10.1007/s10853-015-9705-6)
- [20] Boland CS, Khan U, Ryan G, Barwich S, Charifou R, Harvey A, Backes C, Li Z, Ferreira MS, Mobius ME, Young RJ, Coleman JN (2016) Sensitive electromechanical sensors using viscoelastic graphene-polymer nanocomposites. *Science* 354:1257–1260. doi:[10.1126/science.aag2879](https://doi.org/10.1126/science.aag2879)
- [21] Papageorgiou DG, Kinloch IA, Young RJ (2016) Hybrid multifunctional graphene/glass-fibre polypropylene composites. *Compos Sci Technol* 137:44–51. doi:[10.1016/j.compscitech.2016.10.018](https://doi.org/10.1016/j.compscitech.2016.10.018)
- [22] Kim H, Miura Y, Macosko CW (2010) Graphene/polyurethane nanocomposites for improved gas barrier and electrical conductivity. *Chem Mater* 22:3441–3450. doi:[10.1021/cm100477v](https://doi.org/10.1021/cm100477v)
- [23] Araby S, Meng Q, Zhang L, Kang H, Majewski P, Tang Y, Ma J (2014) Electrically and thermally conductive elastomer/graphene nanocomposites by solution mixing. *Polymer* 55:201–210. doi:[10.1016/j.polymer.2013.11.032](https://doi.org/10.1016/j.polymer.2013.11.032)
- [24] Sadasivuni K, Saiter A, Gautier N, Thomas S, Grohens Y (2013) Effect of molecular interactions on the performance of poly(isobutylene-co-isoprene)/graphene and clay nanocomposites. *Colloid Polym Sci* 291:1729–1740. doi:[10.1007/s00396-013-2908-y](https://doi.org/10.1007/s00396-013-2908-y)
- [25] Chen B, Ma N, Bai X, Zhang H, Zhang Y (2012) Effects of graphene oxide on surface energy, mechanical, damping and thermal properties of ethylene-propylene-diene rubber/petroleum resin blends. *RSC Adv* 2:4683–4689. doi:[10.1039/c2ra01212j](https://doi.org/10.1039/c2ra01212j)
- [26] Zhan Y, Lavorgna M, Buonocore G, Xia H (2012) Enhancing electrical conductivity of rubber composites by constructing interconnected network of self-assembled graphene with latex mixing. *J Mater Chem* 22:10464–10468. doi:[10.1039/C2JM31293J](https://doi.org/10.1039/C2JM31293J)
- [27] Zhan Y, Wu J, Xia H, Yan N, Fei G, Yuan G (2011) Dispersion and exfoliation of graphene in rubber by an ultrasonically-assisted latex mixing and in situ reduction process. *Macromol Mater Eng* 296:590–602. doi:[10.1002/mame.201000358](https://doi.org/10.1002/mame.201000358)
- [28] Potts JR, Shankar O, Du L, Ruoff RS (2012) Processing–morphology–property relationships and composite theory analysis of reduced graphene oxide/natural rubber nanocomposites. *Macromolecules* 45:6045–6055. doi:[10.1021/ma300706k](https://doi.org/10.1021/ma300706k)
- [29] Scherillo G, Lavorgna M, Buonocore GG, Zhan YH, Xia HS, Mensitieri G, Ambrosio L (2014) Tailoring assembly of

- reduced graphene oxide nanosheets to control gas barrier properties of natural rubber nanocomposites. *ACS Appl Mater Interfaces* 6:2230–2234. doi:[10.1021/am405768m](https://doi.org/10.1021/am405768m)
- [30] Potts JR, Shankar O, Murali S, Du L, Ruoff RS (2013) Latex and two-roll mill processing of thermally-exfoliated graphite oxide/natural rubber nanocomposites. *Compos Sci Technol* 74:166–172. doi:[10.1016/j.compscitech.2012.11.008](https://doi.org/10.1016/j.compscitech.2012.11.008)
- [31] Hernández M, Bernal MdM, Verdejo R, Ezquerro TA, López-Manchado MA (2012) Overall performance of natural rubber/graphene nanocomposites. *Compos Sci Technol* 73:40–46. doi:[10.1016/j.compscitech.2012.08.012](https://doi.org/10.1016/j.compscitech.2012.08.012)
- [32] Das A, Kasaliwal GR, Jurk R, Boldt R, Fischer D, Stöckelhuber KW, Heinrich G (2012) Rubber composites based on graphene nanoplatelets, expanded graphite, carbon nanotubes and their combination: a comparative study. *Compos Sci Technol* 72:1961–1967. doi:[10.1016/j.compscitech.2012.09.005](https://doi.org/10.1016/j.compscitech.2012.09.005)
- [33] Wu J, Xing W, Huang G, Li H, Tang M, Wu S, Liu Y (2013) Vulcanization kinetics of graphene/natural rubber nanocomposites. *Polymer* 54:3314–3323. doi:[10.1016/j.polymer.2013.04.044](https://doi.org/10.1016/j.polymer.2013.04.044)
- [34] Yang H, Liu P, Zhang T, Duan Y, Zhang J (2014) Fabrication of natural rubber nanocomposites with high graphene contents via vacuum-assisted self-assembly. *RSC Adv* 4:27687–27690. doi:[10.1039/c4ra02950j](https://doi.org/10.1039/c4ra02950j)
- [35] Ozbas B, O'Neill CD, Register RA, Aksay IA, Prud'homme RK, Adamson DH (2012) Multifunctional elastomer nanocomposites with functionalized graphene single sheets. *J Polym Sci Part B Polym Phys* 50:910–916. doi:[10.1002/polb.23080](https://doi.org/10.1002/polb.23080)
- [36] Ozbas B, Toki S, Hsiao BS, Chu B, Register RA, Aksay IA, Prud'homme RK, Adamson DH (2012) Strain-induced crystallization and mechanical properties of functionalized graphene sheet-filled natural rubber. *J Polym Sci Part B Polym Phys* 50:718–723. doi:[10.1002/polb.23060](https://doi.org/10.1002/polb.23060)
- [37] Xing W, Wu J, Huang G, Li H, Tang M, Fu X (2014) Enhanced mechanical properties of graphene/natural rubber nanocomposites at low content. *Polym Int* 63:1674–1681. doi:[10.1002/pi.4689](https://doi.org/10.1002/pi.4689)
- [38] Schopp S, Thomann R, Ratzsch KF, Kerling S, Altstadt V, Mulhaupt R (2014) Functionalized graphene and carbon materials as components of styrene-butadiene rubber nanocomposites prepared by aqueous dispersion blending. *Macromol Mater Eng* 299:319–329. doi:[10.1002/mame.201300127](https://doi.org/10.1002/mame.201300127)
- [39] Boland CS, Khan U, Backes C, O'Neill A, McCauley J, Duane S, Shanker R, Liu Y, Jurewicz I, Dalton AB, Coleman JN (2014) Sensitive, high-strain, high-rate bodily motion sensors based on graphene-rubber composites. *ACS Nano* 8:8819–8830. doi:[10.1021/Nn503454h](https://doi.org/10.1021/Nn503454h)
- [40] Matos CF, Galebeck F, Zarbin AJ (2014) Multifunctional and environmentally friendly nanocomposites between natural rubber and graphene or graphene oxide. *Carbon* 78:469–479. doi:[10.1016/j.carbon.2014.07.028](https://doi.org/10.1016/j.carbon.2014.07.028)
- [41] Papageorgiou DG, Kinloch IA, Young RJ (2015) Graphene/elastomer nanocomposites. *Carbon* 95:460–484. doi:[10.1016/j.carbon.2015.08.055](https://doi.org/10.1016/j.carbon.2015.08.055)
- [42] Li ZL, Young RJ, Kinloch IA, Wilson NR, Marsden AJ, Raju APA (2015) Quantitative determination of the spatial orientation of graphene by polarized Raman spectroscopy. *Carbon* 88:215–224. doi:[10.1016/j.carbon.2015.02.072](https://doi.org/10.1016/j.carbon.2015.02.072)
- [43] Li ZL, Young RJ, Wilson NR, Kinloch IA, Valles C, Li Z (2016) Effect of the orientation of graphene-based nanoplatelets upon the Young's modulus of nanocomposites. *Compos Sci Technol* 123:125–133. doi:[10.1016/j.compscitech.2015.12.005](https://doi.org/10.1016/j.compscitech.2015.12.005)
- [44] Maire E, Withers PJ (2014) Quantitative X-ray tomography. *Int Mater Rev* 59:1–43. doi:[10.1179/1743280413Y.0000000023](https://doi.org/10.1179/1743280413Y.0000000023)
- [45] Zhang X, Aliasghari S, Nemcova A, Burnett TL, Kubena I, Smid M, Thompson GE, Skeldon P, Withers PJ (2016) X-ray computed tomographic investigation of the porosity and morphology of plasma electrolytic oxidation coatings. *ACS Appl Mater Interfaces* 8:8801–8810. doi:[10.1021/acsami.6b00274](https://doi.org/10.1021/acsami.6b00274)
- [46] Evans JE, Friedrich H, Bals S, Bradley RS, Dahmen T, De Backer A, de Jonge N, Elbaum M, Goris B, Houben L, Leary RK, Midgley PA, Slusallek P, Trappert P, Van Aert S, Van Tendeloo G, Withers PJ, Wolf SG (2016) Advanced tomography techniques for inorganic, organic, and biological materials. *MRS Bull* 41:516–524. doi:[10.1557/mrs.2016.134](https://doi.org/10.1557/mrs.2016.134)
- [47] Young RJ, Lovell PA (2013) Introduction to polymers, 3rd edn. CRC Press, Boca Baton
- [48] Gong L, Kinloch IA, Young RJ, Riaz I, Jalil R, Novoselov KS (2010) Interfacial stress transfer in a graphene monolayer nanocomposite. *Adv Mater* 22:2694–2697. doi:[10.1002/adma.200904264](https://doi.org/10.1002/adma.200904264)